

The effect of Ta oxygen scavenger layer on HfO₂-based resistive switching behavior: thermodynamic stability, electronic structure, and low-bias transport

X. Zhong

Materials Science Division, Argonne National Laboratory, Lemont, Illinois 60439, USA

I. Rungger

Materials Division, National Physical Laboratory, Teddington, TW11 0LW, United Kingdom

P. Zapol

Materials Science Division, Argonne National Laboratory, Lemont, Illinois 60439, USA

H. Nakamura and Y. Asai

Nanosystem Research Institute (NRI), RICS, National Institute of Advanced Industrial Science and Technology (AIST), Central 2, Umezono 1-1-1, Tsukuba, Ibaraki, 305-8568, Japan

O. Heinonen*

Materials Science Division, Argonne National Laboratory, Lemont, Illinois 60439, USA and Northwestern-Argonne Institute for Science and Engineering, Northwestern University, 2145 Sheridan Rd., Evanston, Illinois 60208, USA

Reversible resistive switching between high-resistance and low-resistance states in metal-oxide-metal heterostructures makes them very interesting for applications in random access memories. While recent experimental work has shown that inserting a metallic "oxygen scavenger layer" between the positive electrode and oxide improves device performance, the fundamental understanding of how the scavenger layer modifies heterostructure properties is lacking. We use density functional theory to calculate thermodynamic properties and conductance of TiN/HfO₂/TiN heterostructures with and without Ta scavenger layer. First, we show that Ta insertion lowers the formation energy of low-resistance states. Second, while the Ta scavenger layer reduces the Schottky barrier height in the high-resistance state by modifying the interface charge at the oxide-electrode interface, the heterostructure maintains a high resistance ratio between high- and low-resistance states. Finally, we show that the low-bias conductance of device on-states becomes much less sensitive to the spatial distribution of oxygen removed from the HfO₂ in the presence of the Ta layer. By providing fundamental understanding of the observed improvements with scavenger layers, we open a path to engineer interfaces with oxygen scavenger layers to control and enhance device performance. In turn, this may enable the realization of a non-volatile low-power memory technology with concomitant reduction in energy consumption by consumer electronics and significant benefits to society. energy consumption by consumer electronics and significant benefits to society.

I. INTRODUCTION

Memristive switching devices are candidates for the next-generation fast, scalable, non-volatile, low-power memories [1]. A typical device structure consists of an insulating metal oxide layer sandwiched between two electrodes, forming a metal-insulator-metal (MIM) heterostructure. While the as-deposited device is usually insulating, a low resistance state (the on-state) can be achieved after an "electroforming" process [2]. This is essentially a controlled soft dielectric breakdown during which conducting pathways are formed under the application of an electric field. The device can subsequently be switched reversibly between the low-resistance on-state and a high-resistance off-state using voltage or current pulses. In most devices that depend on the movement of anions, oxygen has a relatively high mobility[1] and the

switching is understood to be caused by the migrating of oxygen from oxide to electrodes. In this work, we will focus on elucidating electrode-oxide interface properties in both low and high resistance states.

Many oxide-electrode materials combinations exhibit memristive switching, most of which do not satisfy requirements for implementation in commercial devices. The TiN-HfO₂ combination is a promising one because of its high scalability, and also because of very mature fabrication technologies based on decades of experience in processing both TiN and HfO₂ in the semiconductor industry. Achieving a robust and high (typically several orders of magnitude) on-off ratio (the ratio of the resistance in the high-resistance off-state to that of the low-resistance on-state) is essential for reliable commercial memories, but in TiN-HfO₂-TiN heterostructures the on-state conductance is low and is characterized as semiconducting, *i.e.*, the conductivity is highly temperature-dependent[3].

Recently, it has been observed that the memristive

* heinonen@anl.gov

switching properties of the TiN-HfO₂-TiN structure can be greatly improved by inserting an “oxygen scavenger” metal layer (*e.g.*, Hf) between TiN and HfO₂ [3, 4]. The on-state current has been shown to be enhanced by three orders of magnitude with little temperature dependence. It has been proposed that oxygen scavenger layers help increase the oxygen vacancy (Vo) concentration inside HfO₂, which in turn facilitates conducting filament formation [3]. The observed improved conductivity by inserting an oxygen scavenger layer strongly suggests the importance of rational design of electrodes for better device performance[5].

In order to control device performance it is essential to understand in detail the device structure-properties relationship. However, characterization of the whole MIM device with atomic resolution is in general difficult [6] and has not been performed in previous works on HfO₂-TiN [3, 4, 7, 8]. In this work, we perform first-principles modeling to elucidate the effects of a thin tantalum layer inserted between the TiN cathode and the HfO₂ oxide layer in TiN-HfO₂ heterostructures. Tantalum is selected because it is also an oxygen scavenger with properties similar to hafnium, and has recently been shown to exhibit stronger electron coupling with HfO₂[9]. The addressed device properties include thermodynamic stability, local chemical composition, electronic structure and transport. The thermodynamic stability of the high- and low-resistance states strongly impacts the device reliability and also strongly influences the local chemical structure of the device. The local chemical structure, in turn, directly determines the electronic structure and transport properties. We first study the thermodynamic stability of several prototypical atomic configurations of both TiN-HfO₂-TiN and TiN-Ta-HfO₂-TiN structures to establish a correlation between atom arrangement and stability of on- and off-states. In particular, we are interested in how oxygen is distributed at the TiN electrode-HfO₂ interface and, possibly, inside the scavenger layer or electrode after oxygen is moved out of HfO₂. Next, we examine the energy band offsets for the modeled MIM structures. The energy band offsets usually profoundly affect the electronic transport properties of the device, especially in the high-resistance off-state. We study how the energy levels of the oxide are shifted when Ta is inserted, and also how they are affected by the location of the diffused oxygen. Finally, we directly correlate the atomic models with the electronic transport properties of the device using a filamentary model for the conductive on-state [5, 9, 10]. Our work shows that the oxygen scavenger layer reduces the formation energy of the conducting state and therefore improves its thermodynamic stability. Furthermore, our results show that the low-resistance state in the presence of a scavenger layer is metallic, which improves the on-off ratio and makes the device performance more robust with much less dependence on temperature, without much dependence on where the oxygen atoms are located in the low-resistance state. These improvements by the insertion of a scavenger layer are important en-

ablers for the realization of non-volatile memory technologies as they may reduce voltage and power requirements for formation and operation, and may improve resistance distributions in low- and high-resistance states. Memory technologies based on resistive switching are interesting not only because their potential scalability and non-volatility. The reduction in electronics power consumption by the introduction of non-volatile memories also has huge benefits for society as a whole. Our work puts the use of scavenger layers as an enabler for resistive switching memory technologies on a firm scientific footing.

II. METHODS

Calculations in the present work are based on Density Functional Theory (DFT) [11, 12] using the Generalized Gradient Approximation (GGA) [13] together with on-site U parameters [14], referred to as GGA+ U , as implemented in the SIESTA/Smeagol electronic structure and transport codes [15–19]. GGA+ U and other advanced DFT methods such as hybrid functionals and Self-Interaction Corrections (SIC) systematically alleviate the problems of underestimating semiconductor band gaps [19–22]. We use norm-conserving pseudopotentials [23] and a plane wave cut-off at 400 Ry; a $2 \times 2 \times 1$ k -point sampling is used for geometry relaxation and transport calculations. To speed up the calculation of these relatively large models, we adopt a single zeta (SZ) basis set for Ti, O and N, and an SZ plus polarization (SZP) basis set for Ta and Hf. We have confirmed that the adopted basis sets yield a good description of the materials geometry (Table I), with the geometry relaxed to residual atomic forces smaller than 0.05 eV/Å.

TABLE I. A comparison of lattice constants in Å calculated using the adopted basis set (SZ and SZP, see text), the default high quality DZP basis set, and measured experimentally.

	TiN	cHfO ₂	Ta
Adopted basis	4.32	5.10	3.36
DZP basis	4.27	5.08	3.32
Experimental	4.25[24]	5.12[25]	3.30[26]

In order to minimize interface strain of the repeating unit cell (see Fig. 1), the (110) direction of cubic HfO₂ (cHfO₂), the (100) direction of rock salt TiN, and the (100) direction of Ta in the body-centered cubic phase are aligned with the vertical direction of the device (the electron transport direction), taken to be the \hat{z} -axis. The structure includes 550 atoms: 169 Ti, 169 N, 54 Hf, 108 O, and 50 Ta in one computational unit cell. In the xy -plane, the lattice constants of this unit cell are 10.81 Å along the \hat{x} -axis, and 10.20 Å along \hat{y} -axis, respectively, corresponding to 3×2 unstrained (110) cHfO₂ unit cells. With HfO₂ set at its experimental lattice constants, TiN

is under a strain of +0.1% and -5.6% in the \hat{x} - and \hat{y} -directions, while Ta is under a strain of +3.7% and -2.3% in the \hat{x} - and \hat{y} -directions, respectively[24–26]. Previous calculations[27] indicate that a 5% strain only marginally changes the electrode work function (less than a 0.05 eV change). As a result, the induced strain in the present model because of lattice mismatch is not expected to significantly change the energy band alignment at the interfaces. For transport calculations, we attach semi-infinite TiN to both ends of the computational unit cell.

In addition to requiring a good description of the material geometry, we use three additional criteria to identify optimal U-parameters, 8 (3) eV for the Hf 5d (O 2p) orbitals: (i) The calculated band gap for pristine cHfO₂ is 5.4 eV, in close agreement with the value of 5.2 eV obtained using a much more computationally expensive GW approximation [28]; (ii) The calculated energy level of a neutral single oxygen vacancy in monoclinic HfO₂ (mHfO₂) agrees well with previous experimental and theoretical work [22, 29]; we also predict the neutral vacancy level to be located just below the center of band gap. (We use oxygen vacancies in mHfO₂ for comparison and calibration because, to the best of our knowledge, there are no data available for vacancy levels in cHfO₂.) This is important because we use a linear chain formed by neutral oxygen atoms as a model for a conducting filament, similar to the previous work[9, 10]; and (iii) we obtain a Schottky Barrier Height (SBH) of 2.4 eV for the TiN-HfO₂ interface, in good agreement with reported values of 1.8 to 2.5 eV from experiments[30, 31].

III. RESULTS AND DISCUSSION

A. Thermodynamics and the effect of the oxygen scavenger layer

The modeled virgin TiN-HfO₂ heterostructure with a Ta insertion layer is shown in Figure 1. The virgin structure is the reference structure with stoichiometric HfO₂ and no defects or oxygen vacancies.

We have considered eight prototype states in two equal sets, the first set without a Ta scavenger layer and the second one with the layer (Fig. 2). We will refer to either the TiN electrode in the first set or the TiN-Ta in the second set as “electrode”, and when we speak of the “interface” between the oxide and the electrode, we refer to the oxide-TiN interface in the first set, and the oxide-Ta interface in the second set. Each set of states contains a virgin state with stoichiometric pristine cHfO₂ representing the off-state as a reference. Three atomic configurations within each set are used to represent the on-state. In these on-states a linear oxygen vacancy filament is simulated by removing one adjacent oxygen atom from each of the nine HfO₂ layers. This linear filament model of oxygen vacancy is similar to that adopted for monoclinic HfO₂ (mHfO₂) to study the quantized conductance observed for HfO₂ [8]. The nine removed oxygen atoms are

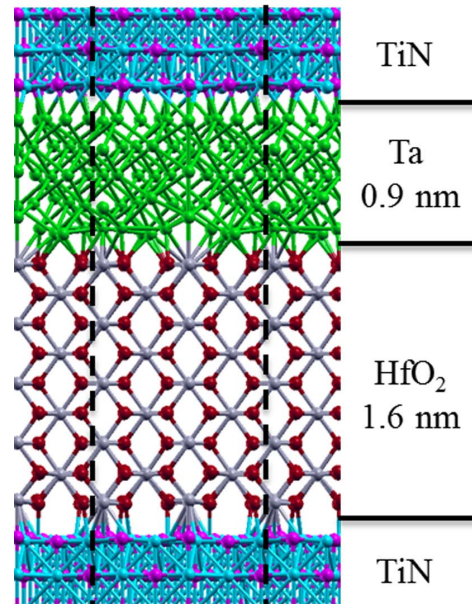


FIG. 1. The relaxed atomic structure of the virgin TiN-HfO₂ device with tantalum layer insertion. The dashed lines show one unit cell used in the modeling. Color scheme: Ti in light blue, N in purple, Ta in green, Hf in grey and O in red.

either simply taken out of device, simulating the oxygen-escaped state (see Table II), or placed at the interface between electrode and HfO₂ (“O at interface” in Table II), or distributed inside the electrode (“O inside electrode” in Table II). These three cases are used to represent three ideal extremes of the device state. The energies per moved oxygen atom of the on-states relative to virgin TiN-cHfO₂-TiN and TiN-cHfO₂-Ta-TiN reference states are summarized in Table II. For each device set (either with or without Ta scavenger layer), the relative energy of one device state (S_i or $S_{i'}$, $i, i' = 2, \dots, 4$) is calculated by the total energy difference between this state and the corresponding virgin state (S_1), i.e., $\Delta E_{S_i} = E_{S_i} - E_{S_1}$, where E_{S_i} and E_{S_1} are the total energies of the given device state and the virgin state, respectively (and analogously for the primed states). Note that for the states 2 and 2' for which oxygen escapes from device, the total energy is calculated by adding the total energy of the remaining device to the formation energy of the oxygen molecules.

When oxygen is placed at the TiN-HfO₂ interface, oxygen atoms move towards HfO₂ and form bonds with Hf during the geometry relaxation process, avoiding the TiN. In contrast, when oxygen atoms are placed at the Ta-HfO₂ interface they move to and bind with Ta (left bottom panel, Fig. 2). As oxygen has a very low solubility in TiN, we model the oxygen inside TiN (Model 4) by calculating the energy of placing one oxygen atom inside TiN bulk (modeled by a cubic box with side length of about 1.1 nm) and multiplying the total energy difference of the model with and without oxygen atom by nine.

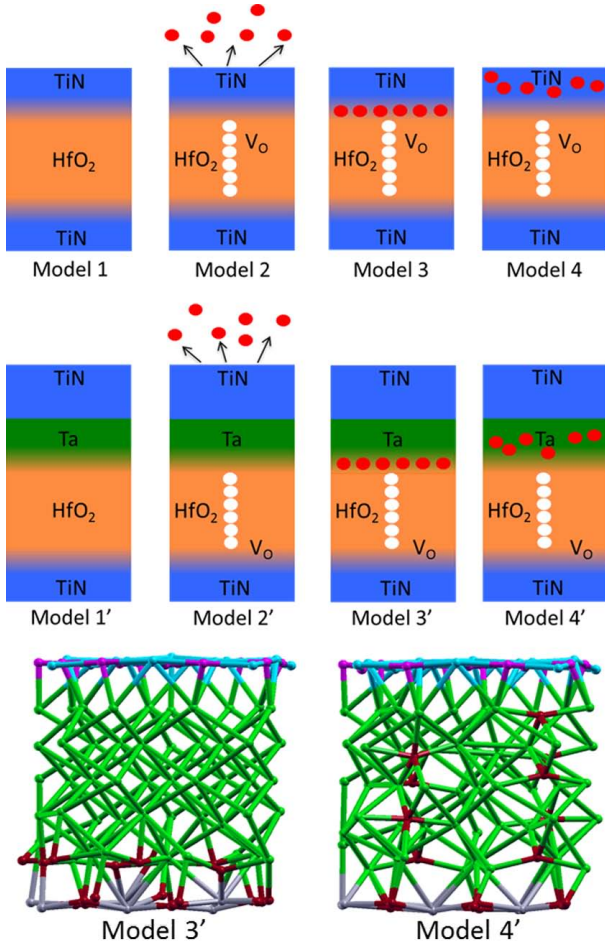


FIG. 2. Top and middle panels: cartoons of the models of memristor device. The top panels depict the TiN-HfO₂-TiN devices without Ta layer. From left to right: the virgin state with pristine HfO₂ (Model 1), oxygen vacancy filament formed in the HfO₂ matrix with oxygen escaping to ambient atmosphere (Model 2), filament formed with oxygen accumulating at the TiN-HfO₂ interface (Model 3) and, filament formed with oxygen distributing uniformly in TiN electrode (Model 4). The middle panel shows the same sequence of oxygen distribution arrangement but with Ta oxygen scavenger layer inserted (Models 1'-4'). The bottom panel shows the atomic structures of the interface region of Models 3' and 4', including one atomic layer of TiN, the Ta inserting layer and one atomic layer of HfO₂ (Ti in light blue, N in purple, Ta in green, Hf in grey and O in red).

For the case where oxygen is distributed inside Ta, oxygen atoms are placed at the interstitial sites in the five Ta layers (right bottom panel, Fig. 2). Our results show that the virgin device state without a conducting filament is the most stable state thermodynamically, with or without Ta scavenger layer (Table II). This implies that an appreciable energy needs to be supplied by electric field to move oxygen from their initial positions in HfO₂.

The hypothetical case of oxygen atoms escaping device and forming O₂ molecules is an endothermic process

TABLE II. Thermostatic stability: the energy difference (in eV) between different device states and reference virgin states. The energy difference is per oxygen atom for nine oxygen atoms removed from the oxide.

	TiN-HfO ₂ -TiN	TiN-Ta-HfO ₂ -TiN
Virgin state (No V _O)	0.00 (Model 1)	0.00 (Model 1')
O escaped	7.40 (Model 2)	7.51 (Model 2')
O at interface	3.63 (Model 3)	2.09 (Model 3')
O inside electrode	8.93 (Model 4)	3.18 (Model 4')

with an energy cost as high as 7.5 eV (per O atom) for the modeled systems, both with and without tantalum layer. The effect of the Ta oxygen scavenger layer is clear if oxygen is assumed to remain in the system without escaping to the atmosphere: when oxygen is moved from HfO₂ to the Ta-HfO₂ interface, the energy cost is calculated to be as low as 2.1 eV. This is less than two thirds of the corresponding energy cost of moving the oxygen to the TiN-HfO₂ interface (3.6 eV). This means a significantly lower cost in energy for removing oxygen from the HfO₂ matrix when the Ta oxygen scavenger layer is inserted. Interestingly, similar trend has been observed experimentally, *i.e.*, by inserting an Hf layer between TiN and HfO₂ the forming bias is reduced from 4 eV to about 2 eV [3].

In contrast, the energy cost for moving oxygen into the TiN electrode is forbiddingly high (8.9 eV), which is even larger than that of oxygen escaping to the ambient atmosphere. Thus, once the interface is saturated with oxygen, further removal of oxygen from the HfO₂ is highly unfavorable, making the formation of an oxygen vacancy filament difficult in a HfO₂-TiN structure without scavenger layer. On the other hand, it is much easier for oxygen to move into Ta, with a much smaller energy cost (3.2 eV) than for moving into TiN. The lower energy cost for moving oxygen into the scavenger layer implies significantly improved switching properties in the presence of the scavenger layer by avoiding oxygen piling up at the electrode-HfO₂ interface, which restrains the formation of an oxygen-deficient phase in HfO₂. The inserted Ta oxygen scavenger layer thus works as a potential trap for oxygen, restraining oxygen from either escaping out of device or moving into the TiN electrode. As a result, oxygen is constrained to the active region near the electrode-oxide interface during device operation, potentially leading to a reduction of device variance and enhanced device endurance.

B. Energy band offsets

We will now discuss the electronic structure of the MIM structures to elucidate the effect of the Ta insertion and location of diffused oxygen on the electronic structure. As we showed in the previous section, the on-states with Ta are favorable thermodynamically over the

on-states without Ta, so we will therefore mostly focus on the on-states with Ta. We will study the virgin states both with and without Ta insertion layer (Models 1 and 1'), the lowest-energy on-state without Ta (Model 3), as well as the on-states with Ta (Models 2', 3' and 4'). We are specifically interested in how the energy levels of the sandwiched oxide are aligned with those of the metallic electrodes for the different prototypical systems.

Our model systems all have nine HfO_2 atomic layers with a total thickness of 1.6 nm sandwiched between electrodes in each model. We first show the band structures we obtained for isolated HfO_2 , both in the stoichiometric form and in the reduced form, in Fig. 3. Note that we will always assign zero of energy to the Fermi level. The electronic states near the Fermi level for the reduced HfO_2 are found to be dominated by vacancy-induced states, which form new mid-gap bands (right panel of Figure 3). As a result, the calculated energy gap is reduced from 5.4 eV to 0.8 eV, and there is a small density of states below the Fermi level but above the valence bands.

We use the projected density of states (PDOS) of the central HfO_2 layer (layer 5) to investigate the electronic structure of the sandwiched HfO_2 ; in contrast with the central layer, the electronic states of the HfO_2 layers in direct contact with the electrodes hybridize with those of the electrodes, such that the local electronic structure and PDOS are strongly influenced by the electrodes. We show the evolution of the PDOS from the interface region to the central HfO_2 bulk region of Models 1 and 3 as examples in Fig. 4. For the first two HfO_2 layers from the interface, layers 1 and 2, the local energy gap is closed even for Model 1, with an appreciable PDOS around the Fermi level (lower panels). From layer 3, the PDOS starts to converge to its values in the bulk region. In Models 2' - 4' each layer in the HfO_{2-x} has a finite density of states (DOS) at the Fermi energy, E_f , indicating metallic properties across the reduced oxide film (not shown). In addition, the contact of HfO_{2-x} with Ta-TiN electrodes appears to induce small but finite PDOS throughout the energy range from the valence band maximum (VBM) to the conduction band minimum (CBM), which effectively closes energy gap as shown for the central layer PDOS in Fig. 5. This implies a weak metallic temperature dependence of the on-state and is consistent with the experimental observation that a scavenger layer reduces the temperature dependence of the on-state[3].

We now address the energy band offset and Schottky barrier height (SBH) by analyzing the PDOS of the sandwiched oxide film (Fig. 5). The device Fermi level is set by the TiN electrodes, which are semi-infinite on both sides of the sandwiched oxide. For the *virgin states* (Models 1 and 1') there is a clear gap of about 5 eV as in bulk HfO_2 (cf. Fig. 3, left panel), but the inserted Ta layer shifts the PDOS downward in energy (Model 1'). The location of the CBM of the oxide with respect to the Fermi level gives the SBH. The SBH are 2.4 and 1.7 eV for Models 1 and 1', respectively, indicating a down-shift of 0.7 eV of the PDOS spectrum upon Ta insertion. For

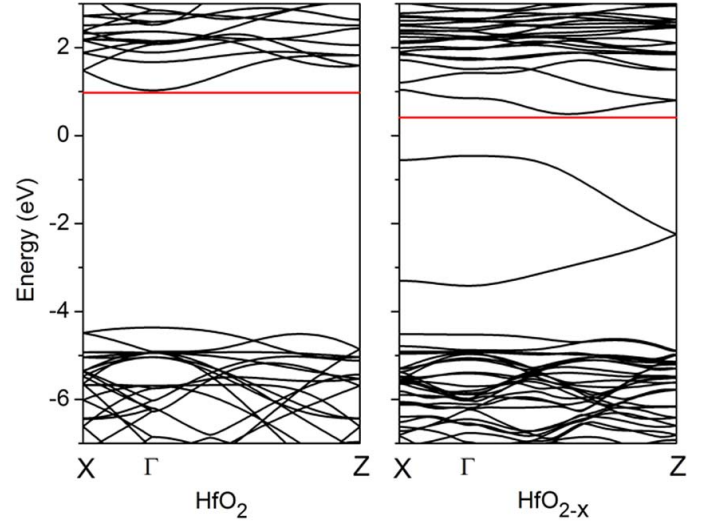


FIG. 3. Electronic band structure of cHfO_2 in the stoichiometric phase (left panel), and with an oxygen vacancy filament formed (right panel). The red lines denote the conduction band minimum (CBM) of both phases.

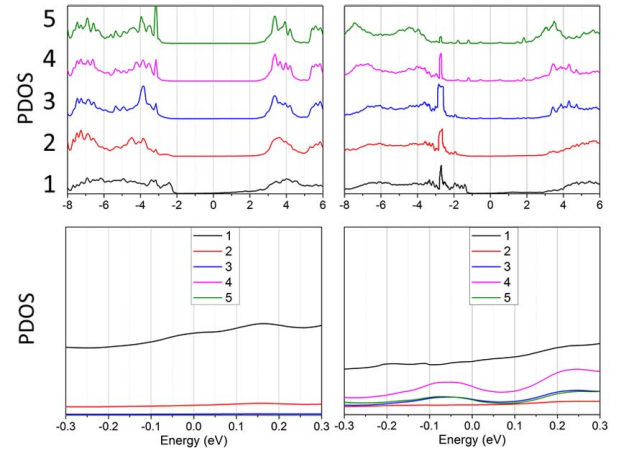


FIG. 4. Projected density of states (PDOS) for Model 1 (left) and Model 3 (right) in arbitrary units. Curves 1 to 5 show the evolution of PDOS from the interface region to the oxide bulk region layer by layer, with layer 1 next to the electrode and layer 5 in the center of the oxide. Adjacent curves in the top graphs are offset vertically by 20 for clarity. The lower panels are the corresponding 20x enlargements around Fermi level (set to zero of energy.)

the on-state Model 3 without Ta, the CBM (and VBM) is shifted down in energy about 1 eV relative to the virgin state (Model 1), and there is a small but non-zero PDOS at the Fermi level E_f , in addition to isolated PDOS peaks below E_f . For the on-states with Ta (Models 2', 3', and 4'), the CBM is shifted down about 1.25 eV compared to the virgin state Model 1'. In addition there appear electron states induced in the gap region as a result of reduction of the HfO_2 . The PDOS at E_f is again finite as in Model 3, which indicates metallic properties. How-

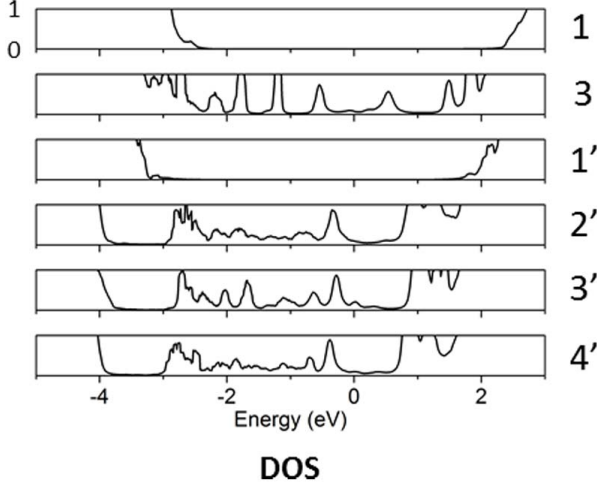


FIG. 5. Electronic structure of the oxide film sandwiched between metal electrodes for models 1, 3, 1' - 4', represented by the PDOS (arbitrary units) of the central oxide atomic layer. For all models we assign zero of energy to the Fermi level.

ever, in contrast with Model 3, there is now a finite PDOS in the entire energy range from CBM (at about 0.75 eV above E_f) to about 3 eV below E_f . We also note that there are no significant differences in the PDOS spectra of Models 2', 3' and 4', with PDOS peaks at approximately the same energies for all these three models. This shows that the energy band offset is insensitive to the distribution of the diffused oxygen atoms in the presence of the Ta oxygen scavenger layer.

Our results are consistent with recent experimental work on the effect of inserting a hafnium layer between TiN and HfO_2 [32]. In Ref. [32] it was observed that the SBH of the TiN- HfO_2 heterostructure was reduced by about 1 eV with the insertion of an Hf inter-layer, and attributed the SBH reduction to a surface dipole induced by oxygen scavenging by the inserted Hf layer. We will now show that our simulation strongly supports this conjecture. We plot the charge distribution across the electrode- HfO_2 interfaces of selected models in Fig. 6. We begin our analysis by discussing Models 1 and 1' [panel (a) in Fig. 6], which contain insulating stoichiometric HfO_2 . The value of the SBH, or more generally, how the energy bands of the oxide are aligned with those of the electrode, is determined by the effective interface dipole [33]. Figure 6 (a) shows that without Ta insertion (Model 1), a negative charge appears on the electrode side, while there is a positive charge on the oxide side. As a result, an interface electric dipole is induced, pointing from electrode to oxide. In contrast, when Ta is inserted (Model 1'), there is a positive charge on the electrode (Ta) side and a negative charge on the oxide side, with the effective electric dipole pointing from oxide to electrode. This reflects the fact Ta has a strong tendency to lose electrons, because of its low electronegativity, com-

pared to TiN. The *net effect* of inserting Ta between TiN and HfO_2 is then a downward shift in energy of the average electrostatic (Hartree) potential energy in Model 1', compared to Model 1, as seen in Fig. 6 (b). This downward shift is about 0.7 eV, which is approximately equal to the downward shift in the SBH from Model 1 to Model 1'. Indeed, we obtain a decrease of 0.7 eV of the SBH of the virgin states [Models 1 and 1', Fig. 5] when Ta is inserted, which is comparable to the experimental value of 1 eV obtained for Hf- HfO_2 [32].

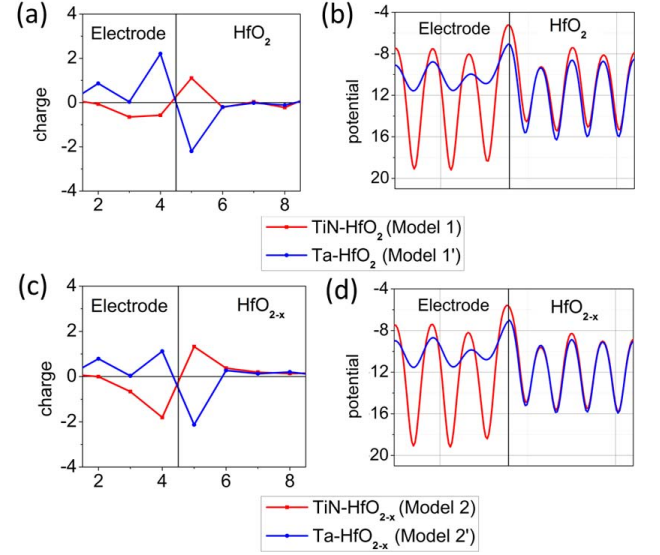


FIG. 6. The charge distribution in electron per square nanometer of each atomic layer across electrode-oxide interface for Model 1 and 1' (a) and for Model 2 and 2' (c). Panel (b) represents the electrostatic (Hartree) potential energy (in eV) for Models 1 and 1', while panel (d) shows the electrostatic potential energy for Models 2 and 2'. For all panels three atomic layers of electrodes and four layers of HfO_2 are plotted. The vertical black lines denote the interface between electrode and HfO_2 .

For the on-states with reduced HfO_2 , inserting Ta has a similar effect on the charge redistribution at the electrode-oxide interface [Fig. 6 (c)]. However, both for Models 2 and 2' the induced charge on the electrode side is reduced (smaller in magnitude for Model 2 and more negative for Model 2') compared to the charge in the virgin states Models 1 and 1'. (We are here using Models 2 and 2' as they provide for a better comparison of what inserting Ta does than the other models with reduced oxide.) However, the electrostatic potential energies rapidly become equal in the reduced oxide [Fig. 6 (d)].

In contrast with stoichiometric HfO_2 , reduced HfO_{2-x} is metallic. When coupled with the electrodes, E_f of HfO_{2-x} and E_f of electrodes must match each other to form the common Fermi level of the device. Thus, the PDOS for HfO_{2-x} shifted in energy relative to that of HfO_2 , with a magnitude of the shift determined by enforcing local charge neutrality. An electric field induced

by an interface dipole is screened by free electrons in HfO_{2-x} . All modeled on-states with Ta show similar energy level alignment between oxide and electrodes (Models 2', 3' and 4', Fig. 5), irrespective of where the diffused oxygen atoms are located. Furthermore, the Ta insertion has little effect on the PDOS for the reduced oxide when the oxygen is not at the oxide-electrode interface, as shown for Models 2 and 2' in Fig. 7. (Oxygen at the TiN-HfO_{2-x} interface, Model 3, severely distorts the interface structure, which affects PDOS below E_f , as seen in Fig. 5.)

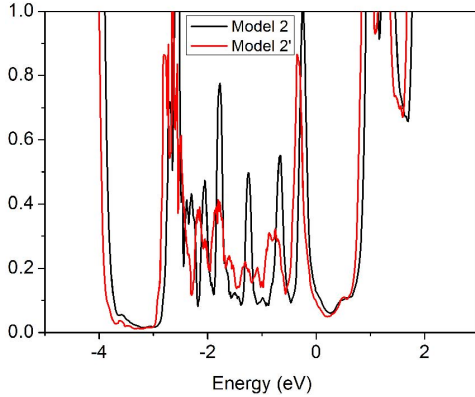


FIG. 7. PDOS of the central HfO_{2-x} layer of Models 2 and 2': for the reduced HfO_{2-x} phase, insertion of Ta has a negligible effect on the energy band offset.

C. Transport properties

Our calculated transmission spectra for the MIM structures (Fig. 8 “Full range”) show a clear correlation with the DOS of the sandwiched oxide film in Fig. 5. For the virgin states, the location of spectrum gap is very similar both in the transmission spectrum and in the PDOS spectrum. The values of the SBH estimated from the transmission spectra are nearly the same as those obtained from PDOS of the central oxide layer. Similarly, for the on-states major transmission peaks have similar locations as the peaks in PDOS across the different models.

TABLE III. The low-bias conductance of various models in unit of the conductance quantum ($G_0 = 2e^2/h$) per nm^2 .

Model	1	1'	2'	3'	4'
Conductance	3.7E-6	5.2E-6	6.3E-2	6.3E-2	3.6E-2

We now discuss the low-bias conductance of selected models. We focus on transmission in an energy range from $E_f - 0.2$ eV to $E_f + 0.2$ eV (Fig. 8 “Around E_f ”). The virgin states show negligible transmission in this energy range, signaling transport only through quantum

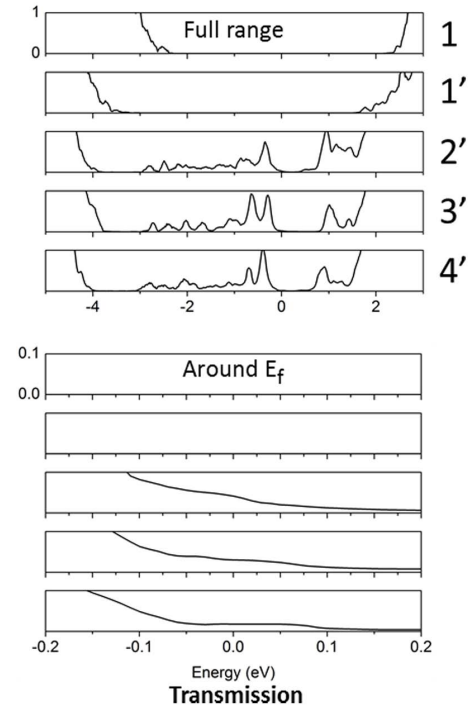


FIG. 8. Electron transmission shown in both expanded energy range (upper panels, “Full range”), and a close-up near E_f (lower panels, “Around E_f ”) in units of the conductance quantum. The zero of energy is set to E_f in both panels.

tunneling. The on-states in contrast show finite transmission at E_f , consistent with metallic properties. In order to quantitatively compare the conductances of the different models, we list their low-bias conductances in Table III, in which the conductance is estimated by averaging the transmission in an energy range from $E_f - 0.2$ to $E_f + 0.2$ eV. For the virgin states, transport under low bias falls into the tunneling regime, with transmission at Fermi level on the order of $10^{-6} G_0$ per nm^2 . Although the SBH is reduced by 0.7 eV when Ta is inserted, the effect on the low-bias transport is small: the estimated conductance of Models 1 and 1' is of the same order of magnitude. The tendency of enhanced tunneling current with reduced SBH when Ta is inserted is offset by electron scattering because of the band mismatch at the additional TiN-Ta interface. This is illustrated in Fig. 9, which compares the transmission functions of two hypothetical structures, both with TiN electrodes. The TiN-TiN-TiN structure consists of a TiN part in the central scattering region, which of course couples seamlessly with two TiN electrodes without any interfacial scattering. As a result, electrons in the whole energy range can be transmitted in a “reflectionless” way, i.e., without any scattering. Therefore, the transmission function for the TiN-TiN-TiN structure just reflects the DOS properties of TiN. In contrast, the mismatch of band structure between Ta and TiN results in a decreased transmission function for the TiN-Ta-TiN structure in the whole en-

ergy range compared to the reflectionless TiN-TiN-TiN structure.

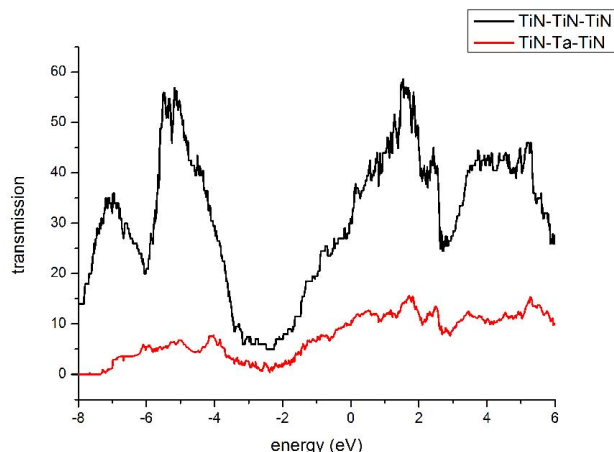


FIG. 9. Electron transmission function of a TiN-Ta-TiN structure (red) and of a reflection-less TiN-TiN-TiN structure (black). The transmission of the TiN-Ta-TiN structure is suppressed because of interfacial scattering because of band mismatch.

For the on-states, all structures (Models 2' to 4') exhibit low-bias conductance on the order of $10^{-2} G_0$ per nm^2 , which is four orders of magnitude greater than that of the virgin states. Thus, the conductivity of the modeled on-states has no strong dependence on the location of diffused oxygen atoms. We note that diffused oxygen either inside Ta or at the Ta-oxide interface induces variations in the magnitude of available PDOS near the Fermi level across HfO_{2-x} layers (Fig. 10). However, each atomic layer has a non-zero PDOS near E_f . As a result, the on-states are metallic, regardless of the location of the diffused oxygen.

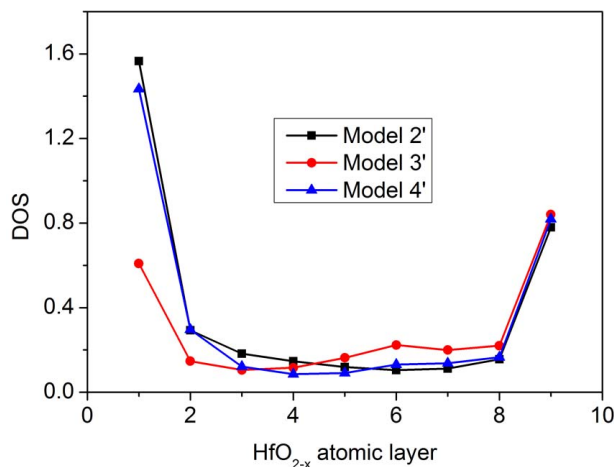


FIG. 10. Evolution of average local PDOS (arbitrary units) across HfO_{2-x} atomic layers, averaged over the energy range between $E_f + 0.2$ eV and $E_f - 0.2$ eV

IV. CONCLUSION

In summary, we have investigated the behavior of TiN-HfO₂-TiN and TiN-HfO₂-Ta-TiN heterostructures with a goal of elucidating the role of the Ta oxygen scavenger layer on thermodynamic stability, electronic structure and transport. We find that the presence of the Ta layer improves the stability of the reduced oxide system, in which oxygen has been depleted from the HfO₂, and facilitates the formation of conducting channel in the oxide, consistent with experimental work[32]. Furthermore, the Ta layer reduces the Schottky barrier height for the insulating system because of a different interface charge at the Ta-HfO₂ interface than at the TiN-HfO₂ interface. Nevertheless, the reduced Schottky barrier height does not negatively impact the on-off ratio. Also, the electronic structure of the reduced oxide with a Ta layer becomes insensitive to the location of the oxygen atoms that are removed from the stoichiometric oxide, with the consequence that the low-bias conductance in the on-state is insensitive to the location of the oxygen atoms. This is in contrast with the structure *without* a Ta layer, for which the electronic structure can vary quite significantly, depending on where the oxygen atoms are located. These results are consistent with experimental observations that a scavenger layer reduces the dispersion of on/off resistance ratio[34].

Our results, which are based on detailed density functional-theory calculations using the GGA+U approximation, explain experimental results[9] that demonstrate better device performance, in particular how the Ta layer facilitates the formation of conducting filaments, and how the Ta layer can lead to more robust devices, that is, less dependence on the microstructure of the device in its on-state. These results provide a firm foundation for further studies of oxygen scavenger layers of different thickness and chemical composition as enablers for realizing low-power resistive random access memory technologies.

ACKNOWLEDGMENTS

The work by X.Z. and O.H. was supported by U. S. DOE, Office of Science under Contract No. DE-AC02-06CH11357. P.Z. acknowledges support from the U.S. Department of Energy, Office of Science, Materials Sciences and Engineering Division. I.R. acknowledges financial support from the European Union's Horizon2020 research and innovation programme within the PETMEM project. We gratefully acknowledge the computing resources provided on Blues and Fusion, high-performance computing clusters operated by the Laboratory Computing Resource Center at Argonne National Laboratory.

-
- [1] J. J. Yang, D. B. Strukov, and D. R. Stewart, *Nat. Nanotechnol.* **8**, 13 (2013).
- [2] J. J. Yang, F. Miao, M. D. Pickett, D. A. A. Ohlberg, D. R. Stewart, C. N. Lau, and R. S. Williams, *Nanotechnology* **20**, 215201 (2009).
- [3] F. D. Stefano, M. Houssa, V. V. Afanas'ev, J. A. Kittl, M. Jurczak, and A. Stesmans, *Thin Solid Films* **533**, 15 (2013), {EMRS} 2012 Symposium L.
- [4] L. Pr  cel, L. Trojman, J. Moreno, F. Crupi, V. Maccaronio, R. Degraeve, L. Goux, and E. Simoen, *J. Appl. Phys.* **114**, 074509 (2013).
- [5] H. Nakamura, T. Miyazaki, K. Nishio, H. Shmia, H. Akinaga, and Y. Asai, in *Computational Electronics (IWCE), 2014 International Workshop on* (2014) pp. 1–3.
- [6] T. Yajima, K. Fujiwara, A. Nakao, T. Kobayashi, T. Tanaka, K. Sunouchi, Y. Suzuki, M. Takeda, K. Kojima, Y. Nakamura, K. Taniguchi, and H. Takagi, *Jpn. J. Appl. Phys.* **49**, 060215 (2010).
- [7] X. Cartoixa, R. Rurali, and J. Su   , *Phys. Rev. B* **86**, 165445 (2012).
- [8] S. Long, X. Lian, C. Cagli, X. Cartoix, R. Rurali, E. Miranda, D. Jimnez, L. Perniola, M. Liu, and J. Su, *Appl. Phys. Lett.* **102**, 183505 (2013).
- [9] T. Miyazaki, H. Nakamura, K. Nishio, H. Shima, H. Akinaga, and Y. Asai, in *JPS Conference Proceedings*, Vol. 1 (2014) p. 2075.
- [10] K. Kamiya, M. Y. Yang, S.-G. Park, B. Magyari-K  pe, Y. Nishi, M. Niwa, and K. Shiraishi, *Appl. Phys. Lett.* **100**, 073502 (2012).
- [11] P. Hohenberg and W. Kohn, *Phys. Rev.* **136**, B864 (1964).
- [12] W. Kohn and L. J. Sham, *Phys. Rev.* **140**, A1133 (1965).
- [13] J. P. Perdew, K. Burke, and Y. Wang, *Phys. Rev. B* **54**, 16533 (1996).
- [14] M. T. Czy  zyk and G. A. Sawatzky, *Phys. Rev. B* **49**, 14211 (1994).
- [15] J. M. Soler, E. Artacho, J. D. Gale, A. Garca, J. Junquera, P. Ordej  n, and D. S  nchez-Portal, *J. Phys. Condens. Matter* **14**, 2745 (2002).
- [16] I. Rungger and S. Sanvito, *Phys. Rev. B* **78**, 035407 (2008).
- [17] A. R. Rocha, V. M. Garcia-Suarez, S. W. Bailey, C. J. Lambert, J. Ferrer, and S. Sanvito, *Nature Mater.* **4**, 335 (2005).
- [18] A. R. Rocha, V. Garcia-Suarez, S. Bailey, C. Lambert, J. Ferrer, and S. Sanvito, *Phys. Rev. B* **73**, 085414 (2006).
- [19] C. D. Pemmaraju, T. Archer, D. S  nchez-Portal, and S. Sanvito, *Phys. Rev. B* **75**, 045101 (2007).
- [20] X. Zhong, I. Rungger, P. Zapol, and O. Heinonen, *Phys. Rev. B* **91**, 115143 (2015).
- [21] S.-G. Park, B. Magyari-K  pe, and Y. Nishi, *Phys. Rev. B* **82**, 115109 (2010).
- [22] P. Broqvist and A. Pasquarello, *Appl. Phys. Lett.* **89**, 262904 (2006).
- [23] N. Troullier and J. L. Martins, *Phys. Rev. B* **43**, 1993 (1991).
- [24] J. Pfl  ger, J. Fink, W. Weber, K. P. Bohnen, and G. Crecelius, *Phys. Rev. B* **30**, 1155 (1984).
- [25] L. Passerini, *Gazz. chim. ital* **60**, 762 (1930).
- [26] Y. Waseda, K. Hirata, and M. Ohtani, *High Temp. High Press.* **7**, 221 (1975).
- [27] Y. J. Oh, A. T. Lee, H.-K. Noh, and K. J. Chang, *Phys. Rev. B* **87**, 075325 (2013).
- [28] H. Jiang, R. I. Gomez-Abal, P. Rinke, and M. Scheffler, *Phys. Rev. B* **81**, 085119 (2010).
- [29] J. L. Gavartin, D. Muoz Ramo, A. L. Shluger, G. Bersuker, and B. H. Lee, *Appl. Phys. Lett.* **89**, 082908 (2006).
- [30] S. Cimino, A. Padovani, L. Larcher, V. Afanasev, H. Hwang, Y. Lee, M. Jurczak, D. Wouters, B. Lee, H. Hwang, and L. Pantisano, *Microelectron. Eng.* **95**, 71 (2012).
- [31] L. R. C. Fonseca and A. A. Knizhnik, *Phys. Rev. B* **74**, 195304 (2006).
- [32] V. V. Afanasev, A. Stesmans, L. Pantisano, S. Cimino, C. Adelman, L. Goux, Y. Y. Chen, J. A. Kittl, D. Wouters, and M. Jurczak, *Appl. Phys. Lett.* **98**, 132901 (2011).
- [33] R. T. Tung, *Appl. Phys. Rev.* **1**, 011304 (2014).
- [34] C. Chen, S. Gao, F. Zeng, G. Tang, S. Li, C. Song, H. Fu, and F. Pan, *J. Appl. Phys.* **114**, 014502 (2013).